

ACCELERATED CO-DESIGN OF ROBOTS THROUGH MORPHOLOGICAL PRETRAINING

005 **Anonymous authors**

006 Paper under double-blind review

ABSTRACT

011 The co-design of robot morphology and neural control typically requires using
 012 reinforcement learning to approximate a unique control policy gradient for each
 013 body plan, demanding massive amounts of training data to measure the perfor-
 014 mance of each design. Here we show that a universal, morphology-agnostic
 015 controller can be rapidly and directly obtained by gradient-based optimization
 016 through differentiable simulation. This process of morphological pretraining al-
 017 lows the designer to explore non-differentiable changes to a robot’s physical lay-
 018 out (e.g. adding, removing and recombining discrete body parts) and immediately
 019 determine which revisions are beneficial and which are deleterious using the pre-
 020 trained model. We term this process “zero-shot evolution” and compare it with
 021 the simultaneous co-optimization of a universal controller alongside an evolving
 022 design population. We find the latter results in *diversity collapse*, a previously
 023 unknown pathology whereby the population—and thus the controller’s training
 024 data—converges to similar designs that are easier to steer with a shared universal
 025 controller. We show that zero-shot evolution with a pretrained controller quickly
 026 yields a diversity of highly performant designs, and by fine-tuning the pretrained
 027 controller on the current population throughout evolution, diversity is not only
 028 preserved but significantly increased as superior performance is achieved. Videos
 029 viewable [at this website](#).

1 INTRODUCTION

031 The co-design of morphology and control in robots is important because robots perform better
 032 when their physical layout is optimized for their intended niche—like a fish out of water, a good
 033 body in one domain can obstruct the acquisition of intelligent behavior in another, if it is unable to
 034 evolve. However, over the past three decades of research, despite exponential increases in comput-
 035 ing power, surprisingly little tangible progress has been achieved beyond the very first co-designed
 036 robots (Sims, 1994). This stagnation is due in part to the nested complexity of evolving a robot’s
 037 morphology and learning a bespoke controller for every morphological variant. Because controllers
 038 are usually optimized in non-differentiable simulations using reinforcement learning (RL), large
 039 amounts of training data are needed to effectively learn a single controller for a single morphol-
 040 ogy, a cost that is compounded by repeatedly relearning new controllers as the robot’s morphology
 041 changes throughout evolution.

042 As a result, the overwhelming majority of prior work has been limited to small numbers of morpho-
 043 logically simple robots that exhibit simple behaviors in simple environments. Even with simplifying
 044 assumptions that significantly speed simulation, such as constraining the design space to infinitely
 045 rigid “stick figures” composed of less than a dozen body parts, there is usually only enough time to
 046 explore a few thousand morphologies (Wang et al., 2019; Zhao et al., 2020; Gupta et al., 2021; Yuan
 047 et al., 2022; Lu et al., 2025; Yu et al., 2025). Others have relaxed this constraint by considering more
 048 flexible bodies composed of many deformable cells (Cheney et al., 2018; Kriegman et al., 2020; Li
 049 et al., 2025), but due in part to the increased computational burden of simulating soft materials, these
 050 robots have had lower motoric complexity (fewer independent motors) and have been much less in-
 051 telligent (completely unresponsive to external stimuli) compared to their rigid bodied counterparts.
 052 Often the robots are restricted to two dimensional worlds (Medvet et al., 2021; Wang et al., 2023b;
 053 Strgar et al., 2024). (See Appx. A.1 for more detailed discussion of this related work.)

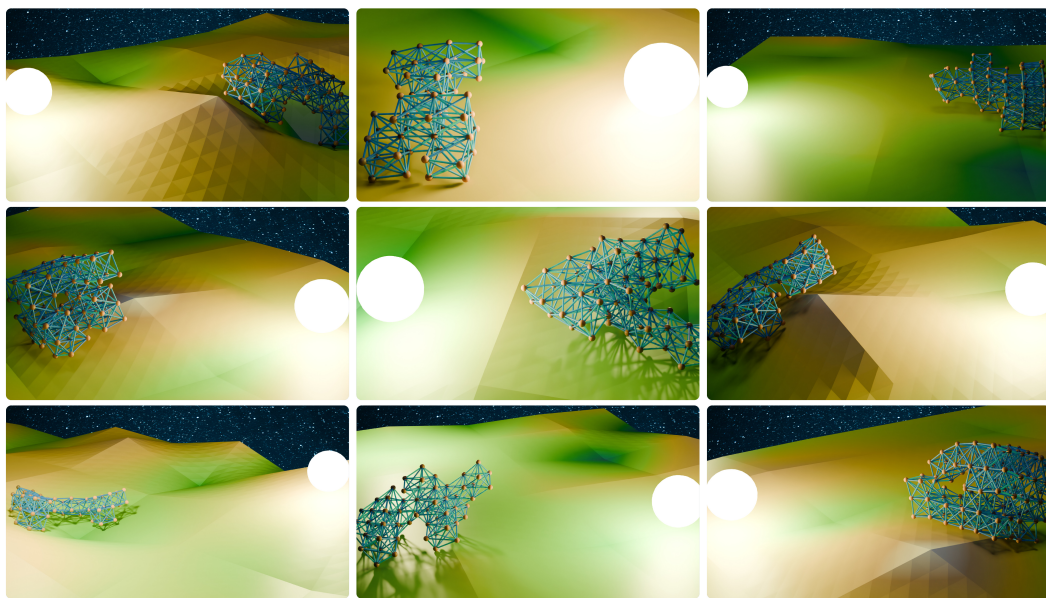


Figure 1: **Universal control of differentiable robots.** Large-scale pretraining and finetuning of a universal controller was achieved by averaging simulation gradients across the robot’s body, world, and goal. The controller is shared by an arbitrarily large and morphologically diverse population of robots as they undergo morphological evolution. The objective is to find designs that can move quickly across a previously-unseen terrain toward a randomly-positioned light source.

Inspired by the remarkable success of large-scale pretrained models in computer vision and natural language processing, we here pretrain a universal controller across millions of complex body plans using gradient information from differentiable simulation, averaging gradients across variations in the robot’s body, world and goal (Fig. 1). Armed with a universal controller, evolution can now iteratively improve the robot’s morphology, and the controller can be rapidly finetuned for the current population with simulation gradients (Fig. 2). This also enables the successful recombination of designs (a.k.a. crossover; Fig. 4), a hallmark of biological evolution and of human engineering that has yet to be convincingly demonstrated in robots.

Indeed there is a tacit assumption in robotics that crossover—the combining of two parent designs to produce offspring—is so unlikely to produce viable offspring, that it is better to omit crossover altogether and focus entirely on small mutations that slightly alter a single design parent to produce offspring. While instances have been reported in which two morphologies were combined using crossover to produce a new morphology (Sims, 1994; Bongard & Pfeifer, 2001; Hiller & Lipson, 2010; Strgar et al., 2024), it was not clear if crossover ever produced offspring with equal or better fitness than either one of their parents—or if the recombined designs were even better than randomly generated robots. Here we show how a pretrained universal controller can unlock successful crossover of robots.

Several cases have been reported in the literature in which RL was used to approximate a universal control policy gradient across a small dataset of previously-designed (Huang et al., 2020; Gupta et al., 2022; Xiong et al., 2023; Bohlinder et al., 2024) or simultaneously co-designed (Schaff & Walter, 2022; Wang et al., 2023b; Li et al., 2025) morphologies. However, the inefficiencies of policy training without recourse to gradient information precluded large-scale pretraining. As we detail below, co-designing morphology and universal control simultaneously from scratch can, and without careful consideration almost certainly will re-

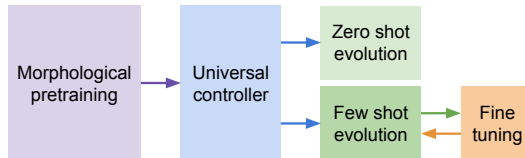


Figure 2: **Overview of the proposed method.** End-to-end differentiable policy training across tens of millions of morphologically distinct robots—morphological pretraining—produces a universal controller, which was kept frozen throughout zero-shot evolution and finetuned for each generation of few-shot evolution.

sult in diversity collapse, inhibiting co-design by reducing it to policy training for a single design. Others (Ma et al., 2021; Matthews et al., 2023; Yuhn et al., 2023; Cochevelou et al., 2023; Strgar et al., 2024) have utilized first-order gradients from differentiable simulation to speed co-design. But, a custom controller still needed to be learned for each morphology, and the resulting robots could only exhibit rote behaviors, such as locomotion in a straight line. (See Appx. A.1.)

Here we demonstrate a more scalable approach that starts with large-scale morphological pretraining in differentiable simulation and yields a **single** morphology-agnostic controller **capable** of adaptive sensor-guided behavior **across evolving populations of distinct**, complex mass-spring robots with hundreds to thousands of independent motors.

2 METHODS

In this section we describe the search space (“morphospace”; Sect. 2.1), the simulator (Sect. 2.2), the universal controller (Sect. 2.3), morphological pretraining (Sect. 2.4), zero shot evolution (Sect. 2.5), few shot evolution with generational finetuning (Sect. 2.6), and simultaneous co-design (Sect. 2.7).

2.1 MORPHOSPACE

Robot morphologies were genetically encoded as contiguous collections of voxels within a $6 \times 6 \times 4$ (Length \times Width \times Height) binary genotype workspace, \mathcal{G} . Voxelized genotypes were then mapped to a phenotype space \mathcal{P} comprising masses \mathcal{M} and springs \mathcal{S} arranged in a cubic lattice with 10 cm³ unit cells (Fig. 3). More specifically, a genotype voxel at position (i, j, k) in \mathcal{G} is expressed phenotypically by eight masses, one in each corner of the corresponding cubic cell in \mathcal{P} with coordinates $(0.1i + \delta_x, 0.1j + \delta_y, 0.1k + \delta_z)$ where $\delta_{x,y,z} \in \{0, 0.1\}$. Springs are then connected to these masses in two patterns: (1) axial springs along cube edges, and (2) planar diagonal springs in each face. Adjacent genotype voxels share masses and springs at their interfaces, ensuring that contiguous structures in \mathcal{G} mapped to cohesive mass-spring networks in \mathcal{P} .

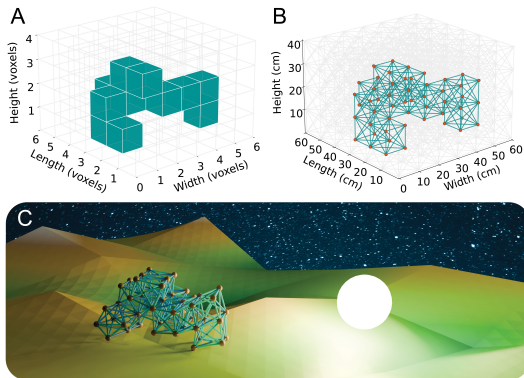


Figure 3: **Genotype to phenotype.** Designs are encoded by a voxel genotype (A), which is expressed as a spring-mass phenotype (B), and evaluated in a differentiable environment (C). Springs (teal lines in B and C) and masses (orange spheres) are motorized and sensorized, respectively.

The resultant $6 \times 6 \times 4$ workspace accommodated a maximum of $|\mathcal{M}| = 245$ potential mass positions and $|\mathcal{S}| = 1648$ potential springs. Each robot was centered in the x-y plane according to its center of mass and shifted to the bottom of the workspace to ensure ground contact prior to behavior. This procedure ensured stable initial conditions for locomotion while maintaining consistent relative positioning between robots of different morphologies.

To identify unique morphologies, we defined an equivalence relation on the genotype space that accounted for translations and symmetries. Two genotypes were considered identical if, after aligning their occupied voxels to the origin, one could be transformed into the other through any combination of: (1) 90° rotations about the z-axis, (2) reflection about the x-axis, or (3) reflection about the y-axis. Each unique design was represented by its lexicographically minimal form across all such transformations.

2.2 DIFFERENTIABLE SIMULATION

We here extend the differentiable 2D mass-spring simulator developed by Strgar et al. (2024) to three dimensions and add extreception: perception of external stimuli outside the body, namely light. Masses on \mathcal{M} hosting photoreceptors were connected by actuating springs on \mathcal{S} (defined in Sect. 2.1), which exerted forces on their endpoint masses to perform phototaxis.

162 During simulation, spring rest lengths may be actuated continuously between $\pm 20\%$ of their initial
 163 values derived from \mathcal{P} (see Sect. 2.1). Spring forces were computed according to Hooke’s law
 164 $F = k(L - L_0)$, where $k = 1.5 \times 10^4$ N/m is the spring stiffness coefficient, L is the current
 165 spring length, and L_0 is the modulated rest length. Resulting impulses, as well as damping and
 166 gravitational forces, were used to update velocities for each mass, and in turn mass positions were
 167 updated using the new velocities.

168 The terrains along which robots behaved were modeled using randomly sampled height maps (see
 169 Appx. A.3 for details). During simulation, terrain heights at arbitrary coordinates (x, y) were com-
 170 puted through bilinear interpolation of the height map. For collision handling, we detected when
 171 a mass’ updated z -coordinate fell below the interpolated terrain height at its (x, y) position. Upon
 172 detection, we employed a three-phase resolution: (1) iterative bisection on the interval $[0, dt]$ to
 173 estimate the time of impact and advance the mass to the contact point, (2) velocity projection onto
 174 the contact surface normal (estimated via central differences), and (3) constrained motion along the
 175 surface tangent for the remaining timestep. Following [Strgar et al. \(2024\)](#), friction forces were com-
 176 puted by negating the tangential velocity component and clamping its magnitude to not exceed the
 177 magnitude of the normal velocity component.

178 Our simulator was implemented in the Taichi programming language ([Hu et al., 2020](#)), providing
 179 both GPU acceleration for parallel, multi-robot simulation and automatic differentiation capabilities.
 180 The simulator was directly integrated with a PyTorch-based universal controller (Sect. 2.3), enabling
 181 end-to-end backpropagation through 1000 timesteps ($dt = 0.004$ s) of physics simulation and neural
 182 control for gradient-based optimization of the controller parameters.

183 2.3 THE UNIVERSAL CONTROLLER

186 We employed a simple multi-layer perceptron (MLP) as a universal controller for adaptive photo-
 187 totaxis: guiding a population of thousands of morphologically diverse robots towards arbitrarily
 188 positioned light sources across randomly varying, rugged terrains. The network mapped two input
 189 streams to spring actuation signals: photosensor readings from masses and central pattern generator
 190 (CPG) inputs. To accommodate all possible body plans in the morphospace (defined in Sect. 2.1),
 191 the network’s input dimension was set to $|\mathcal{M}|$ (the maximum number of masses) and output dimen-
 192 sion to $|\mathcal{S}|$ (the maximum number of springs). Sensors and actuators not present in the a specific
 193 robot’s body had their corresponding signals masked to zero, providing an implicit morphological
 194 conditioning through observation and action space masking.

195 Each mass-bound photosensor measured light intensity following the inverse square law relative
 196 to the light source position. Sensor readings for each robot were normalized by subtracting the
 197 mean computed across that robot’s active (unmasked) sensors, providing a zero-centered, embodied
 198 irradiance gradient. Following [Hu et al. \(2020\)](#), CPG inputs contain five sinusoidal waves with
 199 angular frequency $\omega = 10$ rad/s and phase offsets evenly spaced by $2\pi/5$ radians. Over the 4 sec
 200 simulation period (1000 steps, $dt = 4e^{-3}$ sec), these oscillators completed approximately six cycles.

201 The MLP architecture consisted of an input layer (dim 250: $|\mathcal{M}|$ mass sensors plus 5 CPG inputs),
 202 three hidden layers (dim 256 each), and an output layer (dim 1648: $|\mathcal{S}|$ springs). Each hidden
 203 layer was followed by layer normalization and ReLU activation, while the output layer used a tanh
 204 activation. All layers included learnable biases. In total the model consisted of 620,912 learnable
 205 parameters. Network weights were initialized using a Xavier uniform distribution (gain=1.0) ([Glorot & Bengio, 2010](#)) with zero-initialized biases, and the network was optimized using Adam ([Kingma & Ba, 2015](#)) ($\beta_1 = 0.9$, $\beta_2 = 0.999$) with gradient norm clipping at 1.0. Learning rates were
 206 scheduled using variants of cosine annealing with restarts (detailed in Sects. 2.4, 2.6, and 2.7).

209 2.4 MORPHOLOGICAL PRETRAINING

211 The universal controller was pretrained across a dataset of over 10 million distinct robot morpholo-
 212 gies (see Appx. A.2 for details). The controller was trained over 1400 learning steps to minimize
 213 the batch mean of d_1/d_0 , where d_1 and d_0 represent each robot’s final and initial distances from its
 214 target light source, respectively. This relative distance formulation ensured robots were not penal-
 215 ized for being initialized far from their targets and equally incentivized fine-grained control in robots
 initialized near their targets.

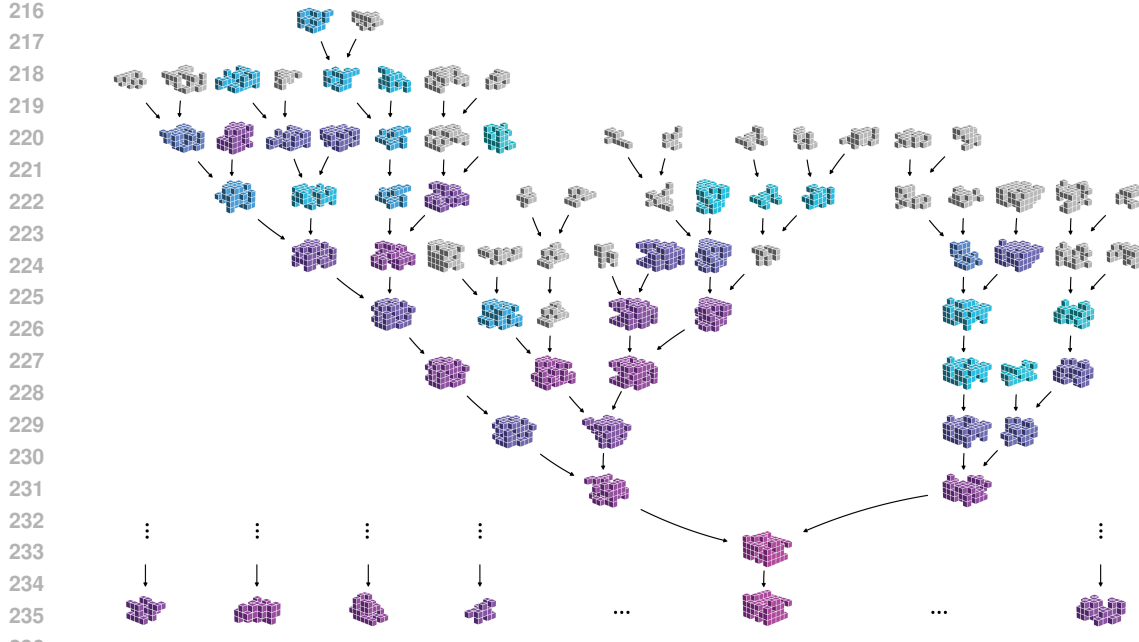


Figure 4: **Few-shot evolution.** A population of 8192 initially random designs (a pair of which are shown in the top row) were randomly recombined and mutated to produce 8192 offspring, temporarily expanding the population to 16384 designs. All designs in the population were driven by the same universal controller, which was rapidly pretrained (before evolution) and finetuned for the current population (at every generation of evolution) using analytical gradients from differentiable simulation. Deleting the worst performing designs and replacing them with the best offspring, and repeating this process for several generations, yields a diversity of increasingly performant designs, and ultimately a final population of 8192 winning designs (bottom row), each with their own unique evolutionary history (phylogeny). An example phylogenetic tree, colored by loss (decreasing from gray to cyan to pink), is shown for one of winning designs.

We used a batch size of 8192, distributed in equal partitions of 1024 across a single compute node consisting of eight H100 SXM GPUs. Each sample consisted of a randomly-generated robot morphology (see Appx. A.2 for details) a randomly-generated terrain shape and a randomly-positioned light source (see Appx. A.3 for details), and was seen exactly once during training. Training used a cosine annealing with restarts schedule, with initial learning rate $1e^{-3}$, cycle length starting at 10 steps and doubling each restart, minimum learning rate $1e^{-5}$, and a decay rate of 0.7 applied to the starting learning rate at each cycle.

2.5 ZERO-SHOT EVOLUTION

Here, we introduce a novel robot design paradigm that leverages a frozen, pretrained universal controller to rapidly evaluate non-differentiable changes to a given robot’s body plan. By using a single, fixed controller for all body plans, the design space may be efficiently explored without the computational burden of training a custom controller for each body plan. We refer to this method as “zero-shot evolution”.

We initialized a population of 8192 random robot morphologies (unseen during pretraining) and evaluated each on a fixed test set of terrain and light source position pairs (see Appx. A.4 for details). A simple genetic algorithm was then applied iteratively: the population produced an equal number of offspring through two variation operators (described below), new offspring were evaluated once on the test set, and the top 50% across parents and offspring (using cached evaluation scores for parents) were selected to form the next generation.

Robot offspring were produced through one of two variation operators: mutation and recombination. The population was partitioned into two distinct groups: a random 25% of members were assigned to produce offspring through mutation, while the remaining 75% were reserved for producing off-

270 spring through recombination (or crossover). Each member in the mutation group produced a single
 271 offspring through random bit flip mutations performed on their genotype. Flips occurred with prob-
 272 ability $p = 1/N$ where $N = 6 \times 6 \times 4$, the total number of voxels in the robot’s genotype. After
 273 mutation, genotypes were processed to ensure validity: only the largest connected component was
 274 retained, and the resulting structure was translated to the bottom center of the workspace. If a muta-
 275 tion produced a body that was either empty or identical to a previously seen body, the process was
 276 repeated with the mutation rate increased by 2.5% until a valid, unique design was obtained.

277 From the recombination group (75% of the
 278 population), pairs of distinct parents were ran-
 279 domly sampled to produce offspring through
 280 crossover (Fig. 5). For each sampled pair,
 281 an offspring’s genotype was created using a
 282 bitwise exclusive or (XOR) operation on the
 283 parent genotypes. As with mutation, post-
 284 processing retained only the largest connected
 285 component and centered it at the bottom of the
 286 workspace. If the resulting design duplicated a
 287 previous one, it was discarded. The sampling
 288 and generation process was repeated until the
 289 number of offspring equaled the size of the re-
 290 combination group (75% of pop).

291 2.6 FEW-SHOT EVOLUTION

293 In this experiment we extend the zero-shot paradigm (described above in Sect. 2.5) by fine-tuning
 294 the pretrained universal controller to the current population at every generation of morphological
 295 evolution. We refer to this approach as “few-shot evolution”. The experimental setup of few-shot
 296 evolution matched the zero-shot case, with one key difference: before evaluation, each generation
 297 received 60 fine-tuning steps (30 for parents, 30 for offspring). The number of fine-tuning steps was
 298 empirically chosen to balance controller adaptation against evolutionary search while maintaining
 299 comparable maximum wall-clock time across experiments. At the start of each generation, the
 300 controller’s weights were reset to their pretrained values and the optimizer state was reinitialized.
 301 Fine-tuning used a cosine annealing learning rate schedule with initial and minimum rates of $3.5e^{-4}$
 302 and $3.5e^{-5}$, respectively. The cycle length was set to 100; however each cycle was truncated to align
 303 each cycle with one generation’s 60 fine-tuning steps resulting in an effective minimum learning rate
 304 of $1.5e^{-4}$. Since every generation re-initialized the pretrained weights, we did not decay the learning
 305 rate at the start of each cycle.

306 2.7 SIMULTANEOUS CO-DESIGN FROM SCRATCH

308 In our third and final experimental group, we remove morphological pretraining and instead sim-
 309 taneously evolve a population of robots and learn their universal controller, from scratch. This is the
 310 algorithm used by Li et al. (2025). Here, it serves as a benchmark of the state of the art (bestowed
 311 with simulation gradients for fair comparison) while also isolating the effect of pretraining through
 312 ablation. Unlike few-shot evolution, controller parameters and optimizer state are inherited across
 313 generations rather than being reset. The genetic algorithm operates as before, but we reduce the
 314 per-generation training to just two learning steps (one for parents, one for offspring) to maintain
 315 parity with our pretraining experiments, where each training batch was unique.

316 Initially, we employed the same cosine annealing learning rate schedule used in morphological pre-
 317 training, but we found it was beneficial to reduce the start-of-cycle learning rate decay factor from
 318 0.7 to 0.65 in order to stabilize learning across cycle restarts in this setting.

319 3 RESULTS

322 In this section we evaluate the results of morphological pretraining (Sect. 3.1), zero- and few shot
 323 evolution (using the pretrained model; Sect. 3.2), and simultaneous co-design from scratch (without
 324 pretraining; Sect. 3.3).

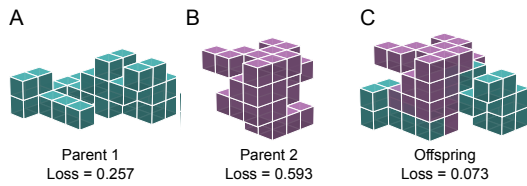


Figure 5: **Recombination of substructures.** A pair of designs (parents; A, B) is combined via crossover to produce a new design (offspring; C) that inherits components from both parents. The pretrained controller enabled several generations of successful recombination events such as this one.

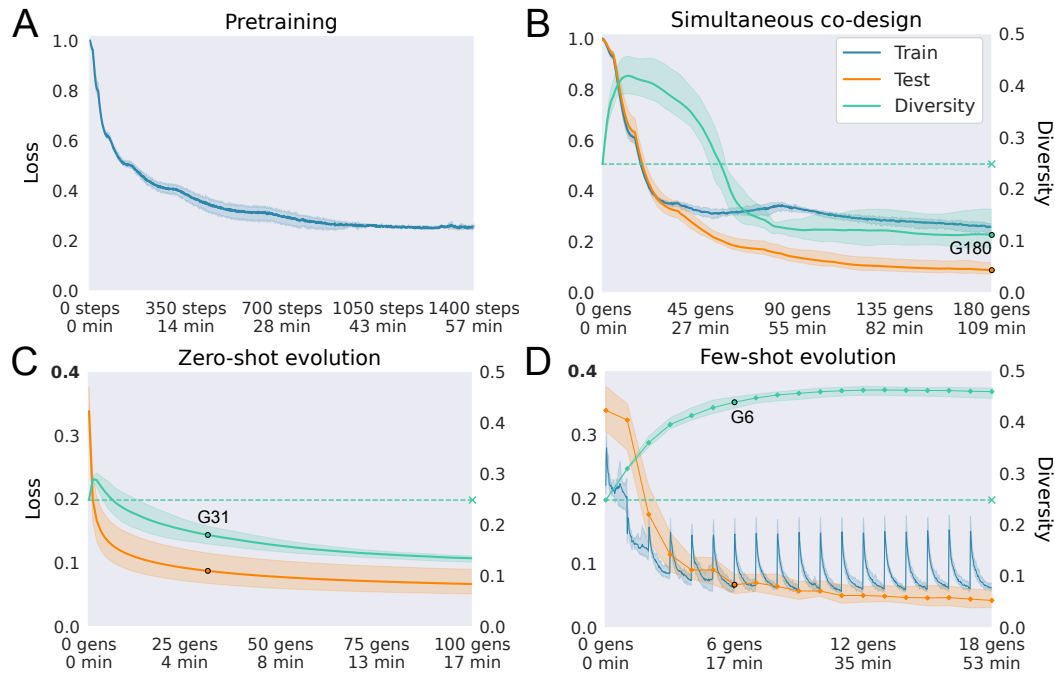


Figure 6: **Performance and diversity.** Morphological pretraining (A) converges with 70% improvement from baseline. The algorithm from Li et al. (2025), simultaneous co-design (from scratch without pretraining; B) achieves similar training loss; but, population diversity (mean pairwise Hamming distance on genotypes) collapses as evolution converges to a single species of similar designs which simplifies shared control. Zero shot evolution (using the pretrained controller; C) rapidly improves test performance, but also suffers diversity collapse as evolution compiles slightly modified clones of the designs that are the most compatible with the pretrained model. Few-shot evolution (D) resets the pretrained controller at the start of each generation and performs 60 finetuning steps per generation. This significantly increases and sustains diversity as well as performance. Solid lines represent the batch (training; blue) or population (test; orange) means, averaged across three independent trials. Shaded regions surrounding the mean curves show the minimum and maximum values across the three trials. Note that pretraining loss (blue curve in A) is not directly comparable to co-design performance (B-D) because designs in the pretraining dataset only served as single-use training samples and were not comprehensively evaluated.

3.1 PRETRAINING PERFORMANCE

Across three independent trials, each using a distinct dataset of randomly-generated morphologies and environments, pretraining exhibited stable learning trajectories with low variance across trials (Fig. 6A), converging in approximately 1,400 learning steps (56 minutes of wall-clock time). Loss was defined as the ratio of final to initial distance from the target light source. At initialization with random controller weights, this ratio was 1.0, indicating robots remained stationary throughout simulation. After pretraining, the loss stabilized at approximately 0.3, representing a 70% improvement. That is, in environments sampled from the training distribution, robots using the pretrained universal controller traversed an average of 70% of their initial distance to the light source. Since each training batch used novel morphologies, we omitted model selection with a validation set.

To visualize the breadth of morphological diversity handled by the pretrained controller, Fig. 11 showcases a representative sample of successful robots. These examples were drawn uniformly from the top-performing 50% of the test morphology set. The sampled bodies exhibit high variation in both body size and shape, demonstrating the non-trivial generalization of the universal controller.

We emphasize that, during pretraining, none of the morphologies used as training samples were ever evaluated. In contrast, zero-shot evolution and few-shot evolution both tested individual morphologies across a set of 10 standardized environments (Appx. A.4). Using the pretrained controller to compare performance of morphologies from the pretraining dataset and morphologies discovered

378 during an application of one of these two algorithms, which employed zero-shot or few-shot design
 379 evaluation, would be inherently confounded.
 380

381 **3.2 ZERO- AND FEW SHOT EVOLUTION (WITH PRETRAINING)**
 382

383 A population of morphologies was evolved through random mutation and crossover operations, us-
 384 ing the pretrained universal controller. On the same challenging set of tasks used for evaluating
 385 pretrained controller generalization, the population converges to near optimal performance in 100
 386 generations of evolution (17 minutes of wall-clock time) without finetuning the controller (“zero
 387 shot evolution”; Sect. 2.5). Although zero-shot evolution shows rapid convergence in controlling
 388 thousands of distinct bodies, this success masks a key pattern: design population diversity decreases
 389 as performance improves. Fig. 6C reveals this pattern—after a brief diversity spike at evolution’s
 390 onset, the population gradually homogenizes. We term this phenomenon diversity collapse, mea-
 391 suring diversity as the population’s mean, pairwise Hamming distance in (and normalized to) the
 392 genotype space \mathcal{G} (defined in Sect. 2.1). This metric naturally reflects differences in morphology
 393 (body) as well as sensing and actuation masking in the universal controller (brain).
 394

395 We found that generational finetuning of the universal controller for the current population (“few
 396 shot evolution”) not only preserves diversity but in fact significantly increases diversity (Fig. 6D).
 397 This is a somewhat surprising result as there was no explicit selection pressure to maintain diver-
 398 sity. The process of morphological evolution seems to intrinsically increase population diversity.
 399 However, in absence of generational finetuning, there is a tipping point at which it is easier to purge
 400 diversity, replacing the worst designs with slightly modified clones of the best, than to discover novel
 401 morphological innovations with superior performance.
 402

403 **3.3 SIMULTANEOUS CO-DESIGN (*without* PRETRAINING)**
 404

405 Ablating pretraining (and finetuning), and instead simultaneously optimizing morphology and uni-
 406 versal control, together from scratch, results once again in rapid diversity collapse (Fig. 6B). Perfor-
 407 mance plateaus in well under 180 generations, corresponding to 360 controller learning steps and
 408 109 minutes of wall-clock time. The extent of diversity collapse can be seen in Fig. 12B, where we
 409 visualize morphologies from one of the three independent trials, and in Fig. 9 where we plot mor-
 410 phological variance across evolved populations in terms of footprint size and body weight. Evolved
 411 populations were extracted from the generation of zero- and few shot evolution (G31 and G6, re-
 412 spectively) at which average loss matched or beat that achieved by simultaneous co-design (G180).
 413

414 In all three co-design paradigms (zero shot, few shot, simultaneous), universal control enabled suc-
 415 cessful crossover (Fig. 8). In terms of offspring survival, crossover was initially more successful
 416 than mutation. But in the case of simultaneous co-design, this was not an apples to apples com-
 417 parison because each generation provided the controller with more time to learn how to control the
 418 population, and the randomly initialized controller was very bad at the task. And so it was not
 419 clear if the success of offspring was due to changes in parent morphology or improvements to the
 420 universal controller. The superior performance of pretraining across random morphologies, shows
 421 that the designs produced by crossover during simultaneous co-design were no better than random
 422 designs. In zero-shot and few-shot evolution, however, the pretrained controller is quite good at the
 423 very start, and in zero-shot the controller is not updated during evolution, providing clear evidence
 424 of successful crossover prior to diversity collapse (Fig. 8).
 425

426 **3.4 GENERALITY OF RESULTS.**
 427

428 While the universal controller was tested out-of-distribution by virtue of morphological evolution,
 429 the above simulation results ignore many of the practical challenges of physical robots, including the
 430 inevitability of component damage and failure. To further assess robustness of the evolved designs
 431 and the generality of the pretrained controller to out-of-distribution morphologies, we incrementally
 432 disabled their sensors and motors (Fig. 14E). On average, designs retained their evolved function-
 433 ality with one quarter of their motors failing and more than half of their sensors failing. Next, we
 434 tested the ability of zero-shot evolution to generalize to novel environments by replacing the con-
 435 tinuously varying terrains seen during pretraining with discrete platforms (Fig. 14B,C). Finally, we
 436 swapped the light source and photoreceptors used during pretraining with magnetic fields and mag-
 437

432 netoreceptors, changing the task from phototaxis to magnetotaxis (Fig. 14D). In both novel terrain
 433 and novel task, zero-shot evolution reshaped the morphologies within the population to meet the new
 434 distributions using the pretrained controller, significantly improving upon pretraining performance
 435 without finetuning.

436

437

438 4 DISCUSSION

439

440 In this paper, we introduced the large-scale pretraining and finetuning of a universal controller using
 441 differentiable simulation and demonstrated how this approach accelerates the design of complex
 442 robots. The learned controller allows most randomly-generated morphologies (mass-spring
 443 networks) to orient along a randomly-generated stimulus (light) vector in three dimensions, and to
 444 follow the vector to its source (phototaxis) across challenging, randomly-generated environments
 445 (terrains)—more or less: some designs were much better than others, and some outright fail (Fig. 7).
 446 Using the pretrained model as a prior, the designer can quickly explore a diversity of changes—from
 447 subtle mutations to large recombinations—across arbitrary numbers of distinct designs in parallel
 448 without destroying the functionality of working designs, and without constantly readapting the con-
 449 troller to support every morphological innovation.

450

451 We intentionally chose a vanilla evolutionary algorithm as “the designer” and a minimal neural
 452 architecture for the universal controller to illustrate the power and potential of our approach. We
 453 were particularly surprised by the effectiveness of a simple MLP in controlling such large numbers of
 454 morphologically complex robots across such challenging terrains. Interestingly, the gaits generated
 455 by the universal controller were quite different from those tailored for individual body plans in
 456 similar conditions (Strgar et al., 2024); instead of walking or ambling across the rugged terrain, the
 457 universal controller discovered patterns of saltation (hopping) not unlike that of kangaroos, in which
 458 coordinated actuation of muscles is followed by an aerial phase.

459

460 It is important to note, however, that while our controller was universal across the robot’s mor-
 461 phology and task environment, we only considered a single material (soft), percept (light), actuator
 462 (linear), and task (phototaxis). Extending this approach to multiple tasks that demand more intricate,
 463 multi-material body plans with multi-modal sensing (e.g. not just moving toward a single stimulus
 464 source, but reacting to various other stimuli, manipulating objects, and working with or against
 465 other robots) may require gradually complexifying the neural architecture. This will likely also re-
 466 quire replacing the direct genotype-to-phenotype mapping with more a sophisticated (pleiotropic)
 467 compression of phenotypes into a latent genome (Li et al., 2025). Instead of presupposing voxel
 468 cells with two dozen springs and eight masses, latent genes could control the expression of more
 469 atomic building blocks, such as individual masses and springs (or subatomic particles within them),
 470 allowing other kinds of non-cubic cells (Hummer & Kriegman, 2024) to emerge. If extended to
 471 self-reconfigurable robots, the latent genome or many such genomes may be expressed in myriad
 472 ways by a single robot with universal self control.

473

474 We also identified in this paper a previously unknown yet inherent problem of co-designing mor-
 475 phology and universal control—diversity collapse—and showed how to solve this problem through
 476 generational finetuning. However, this first investigation of diversity collapse only considered a sin-
 477 gle measure of morphological diversity. Other metrics at both the morphological and behavioral
 478 level could be formulated or derived from a latent genotype space. Such metrics could then be
 479 incorporated into the design algorithm as a constraint or additional objective.

480

481 Another important limitation of this work was that the simulated designs were not transferred to
 482 reality. Doing so may require higher resolution simulations (Fig. 13) or improvements to the simu-
 483 lator, e.g. its model of contact, light, and sensing. Adding noise to these models can also ensure that
 484 the robot’s behavior does not exploit inaccuracies of simulation (Jakobi et al., 1995). The simulator
 485 could also be augmented with a neural network that learns the residual physics (Gao et al., 2024).
 486 However, the universal controller itself might help reduce the simulation-reality gap since it is by
 487 definition insensitive to a wide range of variation in the simulated robot’s body and world.

488

489 Finally, we would like to re-emphasize that results were provided for terrestrial locomotion only,
 490 and it remains to determine whether and how the co-design framework introduced here could be
 491 extended to other behaviors, such as aquatic, aerial, or arboreal locomotion, as well as manipulation.
 492 The latter has been of keen interest in robotics for over a century (Piazza et al., 2019), and in certain

486 instances may require more intricate contacts than movement on land. The differentiable contact
 487 model used by the simulator in this study could, in principle, be extended to object manipulation,
 488 as demonstrated in prior work (Xu et al., 2021; Wang et al., 2023a). Of course, optimizing a single
 489 universal controller for an evolving population of distinct effector morphologies may require a more
 490 complex neural architecture and, in certain cases, may be intractable. Moreover, the algorithms
 491 introduced in this paper require a differentiable simulator is available or can be created, which may
 492 not always be possible.

493 Despite these limitations, the sheer scale and efficiency achieved by this work opens a new frontier
 494 in robot co-design through automatic differentiation, suggesting the breadth of infrastructure and
 495 theory developed in fields of deep learning and neural networks may **in some cases** be leveraged by
 496 robot co-design in future work.

497

498 REFERENCES

500 Jagdeep Bhatia, Holly Jackson, Yunsheng Tian, Jie Xu, and Wojciech Matusik. Evolution gym:
 501 A large-scale benchmark for evolving soft robots. *Advances in Neural Information Processing
 502 Systems (NeurIPS)*, 34:2201–2214, 2021.

503 Nico Bohlinger, Grzegorz Czechmanowski, Maciej Piotr Krupka, Piotr Kicki, Krzysztof Walas, Jan
 504 Peters, and Davide Tateo. One policy to run them all: An end-to-end learning approach to multi-
 505 embodiment locomotion. In *Proceedings of the Conference on Robot Learning (CoRL)*, 2024.

506

507 Josh C Bongard and Rolf Pfeifer. Repeated structure and dissociation of genotypic and phenotypic
 508 complexity in artificial ontogeny. In *Proceedings of the Genetic and Evolutionary Computation
 509 Conference (GECCO)*, pp. 829–836, 2001.

510

511 Nick Cheney, Josh Bongard, Vytas SunSpiral, and Hod Lipson. Scalable co-optimization of mor-
 512 phology and control in embodied machines. *Journal of The Royal Society Interface*, 15(143):
 513 20170937, 2018.

514 François Cochevelou, David Bonner, and Martin-Pierre Schmidt. Differentiable soft-robot gener-
 515 ation. In *Proceedings of the Genetic and Evolutionary Computation Conference (GECCO)*, pp.
 516 129–137. ACM, 2023.

517

518 Junpeng Gao, Mike Y Michelis, Andrew Spielberg, and Robert K Katzschmann. Sim-to-real of soft
 519 robots with learned residual physics. *Robotics and Automation Letters (RA-L)*, 2024.

520

521 Xavier Glorot and Yoshua Bengio. Understanding the difficulty of training deep feedforward neural
 522 networks. In *Proceedings of the International Conference on Artificial Intelligence and Statistics*,
 523 pp. 249–256, 2010.

524

525 Agrim Gupta, Silvio Savarese, Surya Ganguli, and Li Fei-Fei. Embodied intelligence via learning
 526 and evolution. *Nature Communications*, 12(1):1–12, 2021.

527

528 Agrim Gupta, Linxi Fan, Surya Ganguli, and Li Fei-Fei. Metamorph: Learning universal controllers
 529 with transformers. In *Proceedings of the International Conference on Learning Representations
 (ICLR)*, 2022.

530

531 David Ha. Reinforcement learning for improving agent design. *Artificial Life*, 25(4):352–365, 2019.

532

533 Jonathan Hiller and Hod Lipson. Evolving amorphous robots. In *Proceedings of the Conference on
 534 Artificial Life (ALife)*, pp. 717–724, 2010.

535

536 Sunghoon Hong, Deunsol Yoon, and Kee-Eung Kim. Structure-aware transformer policy for inho-
 537 mogeneous multi-task reinforcement learning. In *Proceedings of the International Conference on
 538 Learning Representations (ICLR)*, 2022.

539

Jiaheng Hu, Julian Whitman, Matthew Travers, and Howie Choset. Modular robot design optimiza-
 540 tion with generative adversarial networks. In *Proceedings of the International Conference on
 541 Robotics and Automation (ICRA)*, pp. 4282–4288, 2022.

540 Yuanming Hu, Luke Anderson, Tzu-Mao Li, Qi Sun, Nathan Carr, Jonathan Ragan-Kelley, and
 541 Frédéric Durand. Diffitaichi: Differentiable programming for physical simulation. In *Proceedings*
 542 *of the International Conference on Learning Representations (ICLR)*, 2020.

543

544 Wenlong Huang, Igor Mordatch, and Deepak Pathak. One policy to control them all: Shared modular
 545 policies for agent-agnostic control. In *Proceedings of the International Conference on Machine*
 546 *Learning (ICML)*, pp. 4455–4464, 2020.

547 Tyler Hummer and Sam Kriegman. A non-cubic space-filling modular robot. In *Proceedings of the*
 548 *International Conference on Robotics and Automation (ICRA)*, pp. 2624–2631, 2024.

549

550 Nick Jakobi, Phil Husbands, and Inman Harvey. Noise and the reality gap: The use of simulation in
 551 evolutionary robotics. In *Proceedings of the European Conference on Artificial Life (ECAL)*, pp.
 552 704–720, 1995.

553 Diederik P. Kingma and Jimmy Ba. Adam: A method for stochastic optimization. In *Proceedings*
 554 *of the International Conference on Learning Representations (ICLR)*, 2015.

555 Sam Kriegman, Stephanie Walker, Dylan Shah, Michael Levin, Rebecca Kramer-Bottiglio, and Josh
 556 Bongard. Automated shapeshifting for function recovery in damaged robots. In *Proceedings of*
 557 *Robotics: Science and Systems (RSS)*, 2019.

558

559 Sam Kriegman, Douglas Blackiston, Michael Levin, and Josh Bongard. A scalable pipeline for
 560 designing reconfigurable organisms. *Proceedings of the National Academy of Sciences*, 117(4):
 561 1853–1859, 2020.

562 Sam Kriegman, Douglas Blackiston, Michael Levin, and Josh Bongard. Kinematic self-replication
 563 in reconfigurable organisms. *Proceedings of the National Academy of Sciences*, 118(49):
 564 e2112672118, 2021a.

565

566 Sam Kriegman, Amir Mohammadi Nasab, Douglas Blackiston, Hannah Steele, Michael Levin,
 567 Rebecca Kramer-Bottiglio, and Josh Bongard. Scale invariant robot behavior with fractals. In
 568 *Robotics: Science and Systems (RSS)*, 2021b.

569 Vitaly Kurin, Maximilian Igl, Tim Rocktäschel, Wendelin Boehmer, and Shimon Whiteson. My
 570 body is a cage: the role of morphology in graph-based incompatible control. In *Proceedings of*
 571 *the International Conference on Learning Representations (ICLR)*, 2021.

572 Joel Lehman and Kenneth O Stanley. Evolving a diversity of virtual creatures through novelty search
 573 and local competition. In *Proceedings of the Genetic and Evolutionary Computation Conference*
 574 (*GECCO*), pp. 211–218, 2011.

575

576 Muhan Li, David Matthews, and Sam Kriegman. Reinforcement learning for freeform robot design.
 577 In *Proceedings of the International Conference on Robotics and Automation (ICRA)*, pp. 8799–
 578 8806, 2024.

579 Muhan Li, Lingji Kong, and Sam Kriegman. Generating freeform endoskeletal robots. In *Proceed-*
 580 *ings of the International Conference on Learning Representations (ICLR)*, 2025.

581

582 Haofei Lu, Zhe Wu, Junliang Xing, Jianshu Li, Ruoyu Li, Zhe Li, and Yuanchun Shi. Bodygen: Ad-
 583 vancing towards efficient embodiment co-design. In *Proceedings of the International Conference*
 584 *on Learning Representations (ICLR)*, 2025.

585 Kevin Sebastian Luck, Heni Ben Amor, and Roberto Calandra. Data-efficient co-adaptation of
 586 morphology and behaviour with deep reinforcement learning. In *Proceedings of the Conference*
 587 *on Robot Learning (CoRL)*, pp. 854–869, 2020.

588

589 Pingchuan Ma, Tao Du, John Z Zhang, Kui Wu, Andrew Spielberg, Robert K Katzschnmann, and
 590 Wojciech Matusik. Diffqua: A differentiable computational design pipeline for soft underwater
 591 swimmers with shape interpolation. *ACM Transactions on Graphics (TOG)*, 40(4):1–14, 2021.

592

593 David Matthews, Andrew Spielberg, Daniela Rus, Sam Kriegman, and Josh Bongard. Efficient auto-
 594 matic design of robots. *Proceedings of the National Academy of Sciences*, 120(41):e2305180120,
 2023.

594 Eric Medvet, Alberto Bartoli, Federico Pigozzi, and Marco Rochelli. Biodiversity in evolved voxel-
 595 based soft robots. In *Proceedings of the Genetic and Evolutionary Computation Conference*
 596 (*GECCO*), pp. 129–137, 2021.

597

598 Alican Mertan and Nick Cheney. Towards multi-morphology controllers with diversity and knowl-
 599 edge distillation. In *Proceedings of the Genetic and Evolutionary Computation Conference*
 600 (*GECCO*), pp. 367–376, 2024.

601 Alican Mertan and Nick Cheney. Controller distillation reduces fragile brain-body co-adaptation
 602 and enables migrations in map-elites. *arXiv preprint arXiv:2504.06523*, 2025.

603

604 Emma Stensby Norstein, Frank Veenstra, Kai Olav Ellefsen, Tønnes Nygaard, and Kyrre Glette. Ef-
 605 ffects of compliant and structural parts in evolved modular robots. In *Proceedings of the Artificial*
 606 *Life Conference (ALife)*. MIT Press, 2023.

607 Deepak Pathak, Christopher Lu, Trevor Darrell, Phillip Isola, and Alexei A Efros. Learning to
 608 control self-assembling morphologies: a study of generalization via modularity. In *Advances in*
 609 *Neural Information Processing Systems (NeurIPS)*, 2019.

610

611 Cristina Piazza, Giorgio Grioli, Manuel G Catalano, and Antonio Bicchi. A century of robotic hands.
 612 *Annual Review of Control, Robotics, and Autonomous Systems*, 2(1):1–32, 2019.

613 Charles Schaff and Matthew R Walter. N-limb: Neural limb optimization for efficient morphological
 614 design. *arXiv preprint arXiv:2207.11773*, 2022.

615

616 Charles Schaff, David Yunis, Ayan Chakrabarti, and Matthew R Walter. Jointly learning to con-
 617 struct and control agents using deep reinforcement learning. In *Proceedings of the International*
 618 *Conference on Robotics and Automation (ICRA)*, pp. 9798–9805, 2019.

619 Carmelo Sferrazza, Dun-Ming Huang, Fangchen Liu, Jongmin Lee, and Pieter Abbeel. Body trans-
 620 former: Leveraging robot embodiment for policy learning. *arXiv preprint arXiv:2408.06316*,
 621 2024.

622

623 Karl Sims. Evolving 3D morphology and behavior by competition. *Artificial Life*, 1(4):353–372,
 624 1994.

625

626 Luke Strgar, David Matthews, Tyler Hummer, and Sam Kriegman. Evolution and learning in differ-
 627 entiable robots. In *Proceedings of Robotics: Science and Systems (RSS)*, 2024.

628

629 Frank Veenstra and Kyrre Glette. How different encodings affect performance and diversification
 630 when evolving the morphology and control of 2D virtual creatures. In *Proceedings of the Confer-
 631 ence on Artificial Life (ALife)*, pp. 592–601, 2020.

632

633 Tingwu Wang, Yuhao Zhou, Sanja Fidler, and Jimmy Ba. Neural graph evolution: Towards efficient
 634 automatic robot design. In *Proceedings of the International Conference on Learning Representa-
 635 tions (ICLR)*, 2019.

636

637 Tsun-Hsuan Wang, Juntian Zheng, Pingchuan Ma, Yilun Du, Byungchul Kim, Andrew E. Spielberg,
 638 Joshua B. Tenenbaum, Chuang Gan, and Daniela Rus. Diffusebot: Breeding soft robots with
 639 physics-augmented generative diffusion models. In *Advances in Neural Information Processing*
 640 *Systems (NeurIPS)*, 2023a.

641

642 Yuxing Wang, Shuang Wu, Tiantian Zhang, Yongzhe Chang, Haobo Fu, Qiang Fu, and Xueqian
 643 Wang. Preco: Enhancing generalization in co-design of modular soft robots via brain-body pre-
 644 training. In *Proceedings of the Conference on Robot Learning (CoRL)*, pp. 478–498, 2023b.

645

646 Zheng Xiong, Jacob Beck, and Shimon Whiteson. Universal morphology control via contextual
 647 modulation. In *Proceedings of the International Conference on Machine Learning (ICML)*, pp.
 648 38286–38300, 2023.

649

650 Zheng Xiong, Risto Vuorio, Jacob Beck, Matthieu Zimmer, Kun Shao, and Shimon Whiteson. Dis-
 651 tilling morphology-conditioned hypernetworks for efficient universal morphology control. In
 652 *Proceedings of the International Conference on Machine Learning (ICML)*, 2024.

648 Jie Xu, Tao Chen, Lara Zlokapa, Michael Foshey, Wojciech Matusik, Shinjiro Sueda, and Pulkit
649 Agrawal. An end-to-end differentiable framework for contact-aware robot design. In *Proceedings*
650 *of Robotics: Science & Systems (RSS)*, 2021.

651 Chen Yu, David Matthews, Jingxian Wang, Jing Gu, Douglas Blackiston, Michael Rubenstein, and
652 Sam Kriegman. Reconfigurable legged metamachines that run on autonomous modular legs.
653 *arXiv preprint arXiv:2505.00784*, 2025.

654 Ye Yuan, Yuda Song, Zhengyi Luo, Wen Sun, and Kris Kitani. Transform2Act: Learning a
655 transform-and-control policy for efficient agent design. In *Proceedings of the International Con-*
656 *ference on Learning Representations (ICLR)*, 2022.

657 Changyoung Yuhn, Yuki Sato, Hiroki Kobayashi, Atsushi Kawamoto, and Tsuyoshi Nomura. 4D
658 topology optimization: Integrated optimization of the structure and self-actuation of soft bodies
659 for dynamic motions. *Computer Methods in Applied Mechanics and Engineering*, 414:116187,
660 2023.

661 Allan Zhao, Jie Xu, Mina Konaković-Luković, Josephine Hughes, Andrew Spielberg, Daniela Rus,
662 and Wojciech Matusik. Robogrammar: graph grammar for terrain-optimized robot design. *ACM*
663 *Transactions on Graphics (TOG)*, 39(6):1–16, 2020.

664
665
666
667
668
669
670
671
672
673
674
675
676
677
678
679
680
681
682
683
684
685
686
687
688
689
690
691
692
693
694
695
696
697
698
699
700
701

A APPENDIX

A.1 ADDITIONAL DISCUSSION

As detailed above in the introduction (Sect. 1), all prior work that trained a universal controller did so in a computationally inefficient manner without recourse to gradient information. And all prior work that leveraged simulation gradients to optimize single-morphology locomotion policies only did so for movement in a perfectly straight line without recourse to external perception. The two algorithmic contributions of this paper are thus: (i) end-to-end differentiable training of a universal controller, which enabled large scale pretraining and finetuning of adaptive sensor-guided behavior; and (ii) new co-design algorithms that utilize this pretrained controller to guide discrete morphological optimization. These novel algorithms established for the first time successful design recombination and revealed the previously unknown phenomenon of diversity collapse, the discovery of which is the primary intellectual contribution of this paper.

Previously, under the computational burden of non-differentiable policy training, others (Huang et al., 2020; Gupta et al., 2022; Wang et al., 2023b; Xiong et al., 2023; 2024; Bohlinger et al., 2024) pretrained a universal locomotion policy but it was unclear whether or how it could be used for morphological evolution. Li et al. (2025) co-designed a population of 64 morphologies and a universal controller but did so simultaneously, which as we have shown here, can lead to diversity collapse. Wang et al. (2023b) intentionally collapsed diversity to a single morphology after pretraining a universal controller. Schaff & Walter (2022) co-designed a universal controller for two kinds of body plans (quadrupeds and hexapods), optimizing the length and articulation of rigid links within their presupposed spine and leg pairs, which ultimately “converge[d] toward a single design”. Morphological diversity matters because some designs generalize better than others to novel circumstances (Fig. 14), the details of which may be impossible to simulate or unknowable a priori.

It may also be helpful to situate our work in relation to that of (Ha, 2019; Schaff et al., 2019; Luck et al., 2020), which used RL to co-optimize the neural control and morphological parameters of a presupposed kinematic tree that could not change during optimization. Although the policy could enlarge or reduce the limbs of “a given morphology”, it could not change the overall design: the Ant was always an Ant, with four limbs equally spaced about its torso. Adding and removing body parts was impossible because limb size could not go to zero and new limb buds could not be placed along the Ant. Recombining discrete body parts was impossible because there was not a population of distinct designs to recombine. In short, morphological evolution was impossible. And once again, this prior work treated the simulation as a non-differentiable component of the learning process. Moreover, the resulting controller could only produce blind locomotion in a single, relatively simple body with a small number of degrees of control freedom. Our methods of few-shot and zero-shot evolution, on the other hand, generate a population of thousands of designs with hundreds to thousands of motors that improve performance beyond pretraining in an adaptive, sensor-guided navigation task.

Although discussed above in Sects. 1 and 4, and detailed in Sect. 2.1, it is also worth reiterating that morphospace was here limited to actuated springs and sensorized masses on a regular grid, which is consistent with prior work (Cheney et al., 2018; Kriegman et al., 2020; Medvet et al., 2021; Bhatia et al., 2021; Wang et al., 2023b; Li et al., 2024; Strgar et al., 2024; Mertan & Cheney, 2024; 2025). Following Bhatia et al. (2021), the morphospace of many recent co-design studies have been constrained to a small 2D grid of elastic cells in non-differentiable simulation. We hope that the differentiable 3D simulations released here can provide the basis of a more expressive and scalable benchmark platform for the community.

We stated in Sect. 1 that prior co-design research has mostly focused on simple bodies and behaviors, and one of the goals of our research is to increase complexity in both. The morphologies in this paper have higher motoric complexity (larger numbers of independent motors) than those in prior work, but there are many ways to measure complexity. The endoskeletal robots from Li et al. (2025), for instance, contained fewer motors (and were non-differentiable) but possessed finer grain anatomical complexity (freeform jointed skeletons and soft tissues) than the mass-spring bodies in this paper. We can to some extent scale the anatomical complexity of mass-spring robots by simply increasing their number of springs and masses (Fig. 13), but they would still lack the joint constraints and contact models of Li et al. (2025). And while we benchmarked against the simultaneous co-design algorithm from Li et al. (2025), their genetic encoding and evolutionary strategy is almost certainly more scalable than our direct representation and navigation of morphospace. The

algorithms introduced in this paper are inherently synergistic with this and the many other, diverse approaches to robot topology optimization (Wang et al., 2019; Zhao et al., 2020; Gupta et al., 2021; Kriegman et al., 2021a;b; Hu et al., 2022; Matthews et al., 2023; Li et al., 2024; Yu et al., 2025) including those that also avoid policy retraining for each new morphological variant (Wang et al., 2019; Pathak et al., 2019; Kriegman et al., 2019; Yuan et al., 2022; Schaff & Walter, 2022; Mertan & Cheney, 2024; Lu et al., 2025; Mertan & Cheney, 2025). One of the most promising avenues for future work would be to determine task environments in which it becomes necessary to replace the simple MLP controller used in this paper with one that can better condition behavior on details of the robot’s current morphology through masked attention (Kurin et al., 2021; Hong et al., 2022; Gupta et al., 2022; Sferrazza et al., 2024; Li et al., 2025), hypernetworks (Xiong et al., 2024) or contextual modulation (Xiong et al., 2023). Likewise, the minimal evolutionary algorithm used in this paper to optimize the robot’s discrete topology may be replaced in future by design algorithms that explicitly promote quality diversity (Lehman & Stanley, 2011; Veenstra & Glette, 2020; Norstein et al., 2023; Mertan & Cheney, 2024; 2025) and thereby strive to realize the creativity and open-endedness of biological evolution in robots.

771 A.2 RANDOM ROBOT GENERATION

773 Random morphologies were generated de novo during pretraining and as the initial seed population
 774 of evolution (gen 0). First, we enumerated all possible (length, width, height) tuples with length
 775 and width in $[1, 6]$ and height in $[1, 4]$, corresponding to the voxel dimensions of \mathcal{G} (see Sect. 2.1). We then randomly sampled a volume uniformly from the set of possible volumes and subsequently
 776 sampled a compatible (length, width, height) tuple to define the bounding box for the genotype.
 777 This ensured our dataset contained morphologies of varying volumes and dimensions. Within this
 778 bounding box, all voxels were initialized as inactive (zero) and then randomly activated according to
 779 probability $p \sim \mathcal{N}(\mu = 0.35, \sigma = 0.125)$, clipped to $[0.1, 0.6]$. If the resulting structure contained
 780 no active voxels, sampling was repeated. The largest connected component of active voxels was
 781 retained to ensure a valid morphology. If necessary, the bounding box was zero-padded back to
 782 $6 \times 6 \times 4$ and the connected component was centered in the horizontal plane and shifted to the bottom
 783 of the workspace. The parameters of the sampling distribution were empirically set to produce
 784 diverse structures, a sampling of which can be visualized in Figs. 12A and 11.

785 A.3 RANDOM ENVIRONMENT GENERATION

786 Random environments were generated during pretraining (Sect. 2.4), few-shot evolution (Sect. 2.6)
 787 and simultaneous co-design (Sect. 2.7). Zero-shot evolution did not require random environment
 788 generation since there was no model training involved and thus relied only on evaluation environments
 789 (Appx. A.4). An environment consisted of a (terrain, light source position) tuple. A random terrain was generated by sampling a discrete 8×8 height map of uniformly spaced values.
 790 Each value was sampled independently from a Gaussian distribution $\mathcal{N}(\mu = 0, \sigma = \mathcal{U}(0, 0.1))$.
 791 A light source position was generated by sampling (x, y) coordinates uniformly inside the circle
 792 $(x - r_x)^2 + (y - r_y)^2 = r^2$, where $r \sim \mathcal{U}(0.4, 2.0)$ and (r_x, r_y) was the initial center of mass
 793 position of each robot. Prior to the start of simulation light source positions were placed in 3D by
 794 incorporating the terrain height at the sampled (x, y) location.

795 A.4 EVALUATION ENVIRONMENTS

796 Each generation of zero-shot evolution (Sect. 2.5), few-shot evolution (Sect. 2.6) and simultaneous
 797 co-design (Sect. 2.7), both the parents and their offspring were evaluated on a fixed set of 10 testing
 798 environments. This dataset was constructed as follows. Light sources were placed in two rings
 799 centered about the robot’s starting position: five targets at radius 1.5 and five at radius 2.0, with their
 800 angular positions offset to maximize radial coverage. Terrains were sampled at five uniformly spaced
 801 difficulty levels, characterized by height map standard deviations in $\{0.02, 0.04, 0.06, 0.08, 0.1\}$.
 802 Each ring of light position targets was randomly paired with one terrain from each difficulty level.

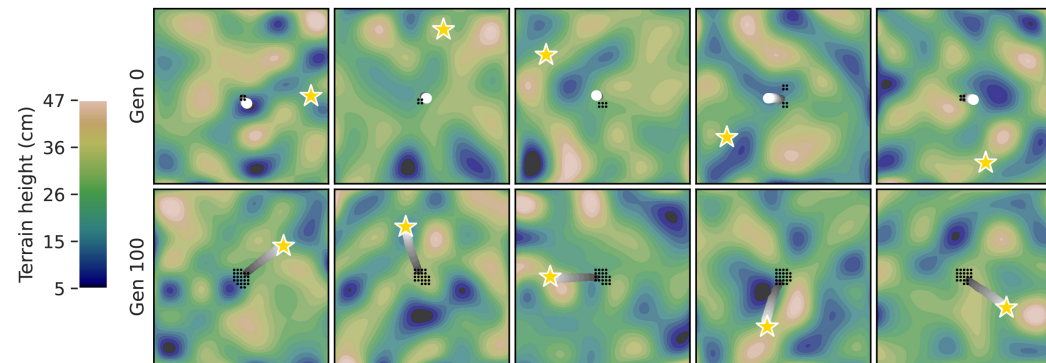
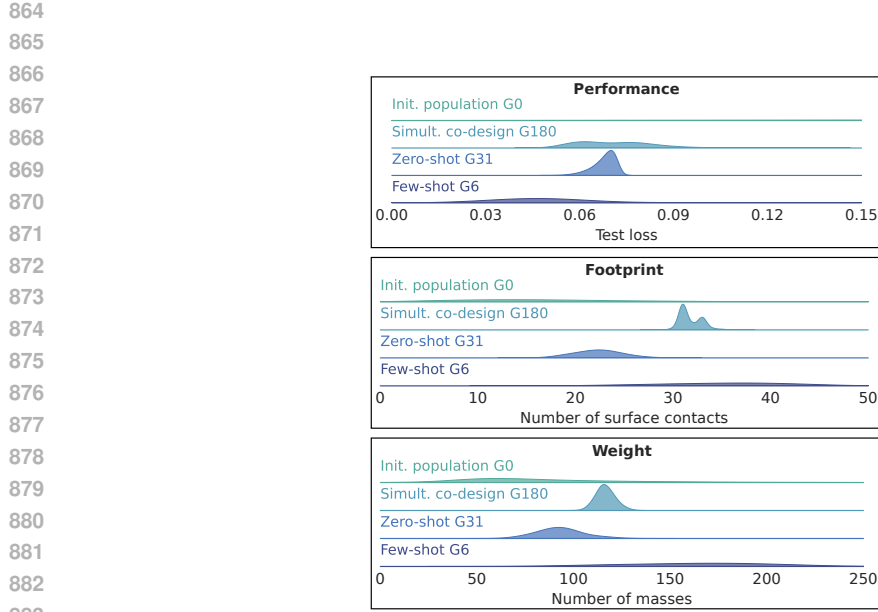


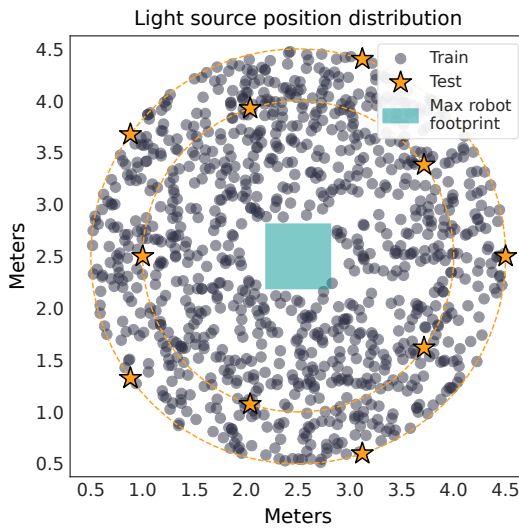
Figure 7: **Evolution of phototaxis.** The five worst designs in the population are depicted before (top row) and after (bottom row) zero-shot evolution. Each design (black dotted footprints) was placed in the center of a randomly generated map. Before evolution, not all of designs in the population could move (gray to white trajectories) across any terrain toward a light source (gold stars) using the pretrained controller. After evolution, they could. One of the design principles that evolution discovered is that larger footprints increase locomotion stability.



Figure 8: **Success of crossover vs. mutation.** The evolutionary success of mutation and crossover is here defined by the fraction of mutation and crossover events from the previous generation that were absorbed into the current population. Early in evolution, the pretrained controller enables greater than 50% crossover success rate. In the first generation of zero shot evolution, for instance, 77% of crossover attempts resulted in offspring that were better than at least one of their parents, and more than half of these offspring were better than both of their parents. After a few generations, mutations that finely tune good designs were less likely to be deleterious than exchanging large components between designs.



884 **Figure 9: Evolved populations.** Population performance, phenotype footprint size, and body mass
885 for the initial (randomly generated) and evolved design populations. Whereas zero-shot evolution
886 shifts the population toward smaller designs that are easier to control with the pretrained policy, few
887 shot evolution maintained a diverse population of overall larger designs with larger footprints which
888 increase locomotion stability.



911 **Figure 10: Phototaxis training and testing.** During pretraining, simult. co-design, and few-shot
912 finetuning, training light source locations (gray circles) were sampled uniformly within a circle cen-
913 tered on the robot's initial position (blue square). At every learning step, a batch of 8192 randomly
914 positioned lights was sampled, and each was paired with a unique, random morphology and random
915 terrain. Test light source locations (orange stars) were identical across all methods for fair compari-
916 son.

917

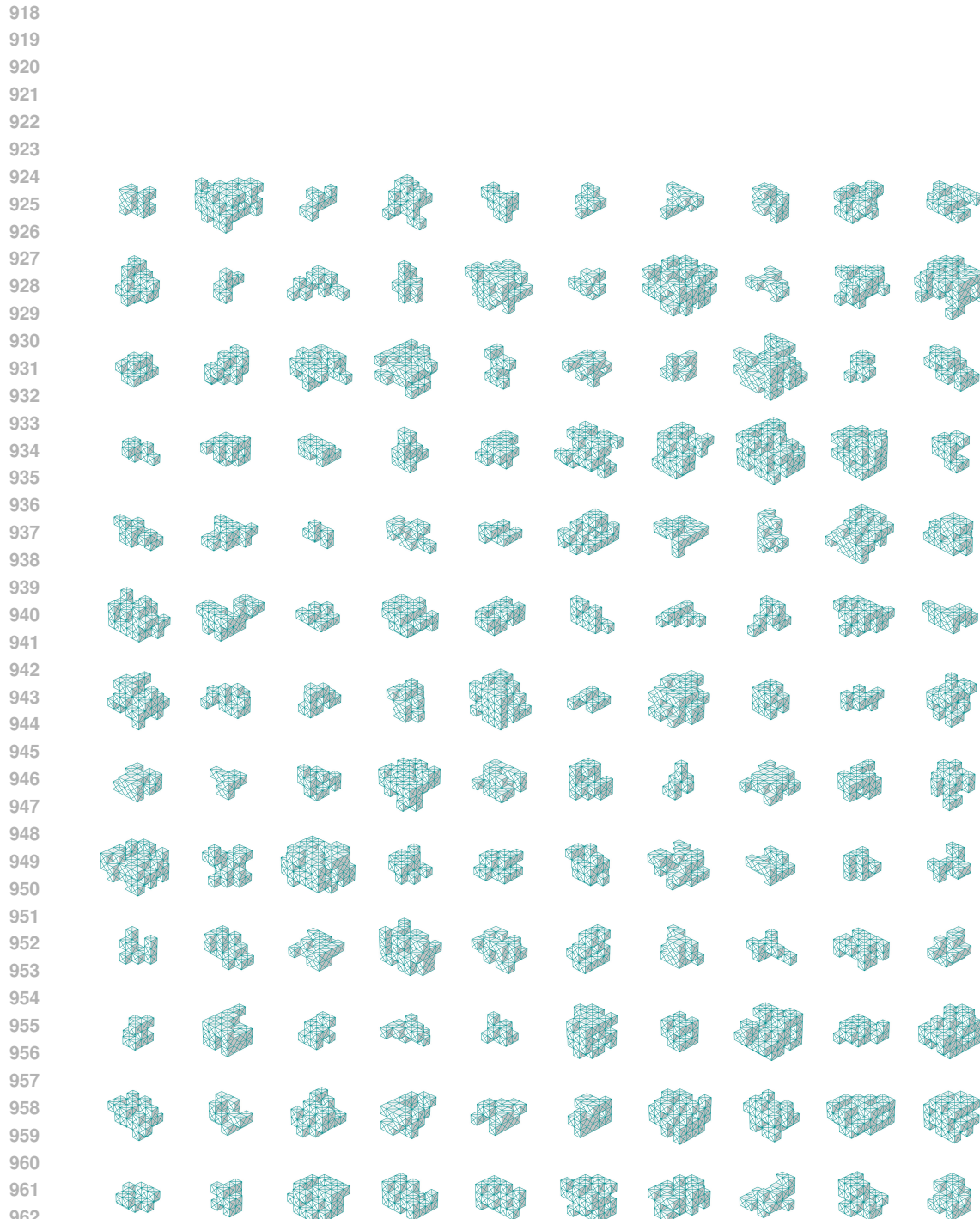


Figure 11: **Generalization of pretrained universal controller.** Randomly sampled morphologies from the top 50% of performers in generation 0 of zero-shot evolution. The universal controller successfully controls these diverse, previously unseen robot designs, demonstrating effective generalization across morphologies.

968
969
970
971

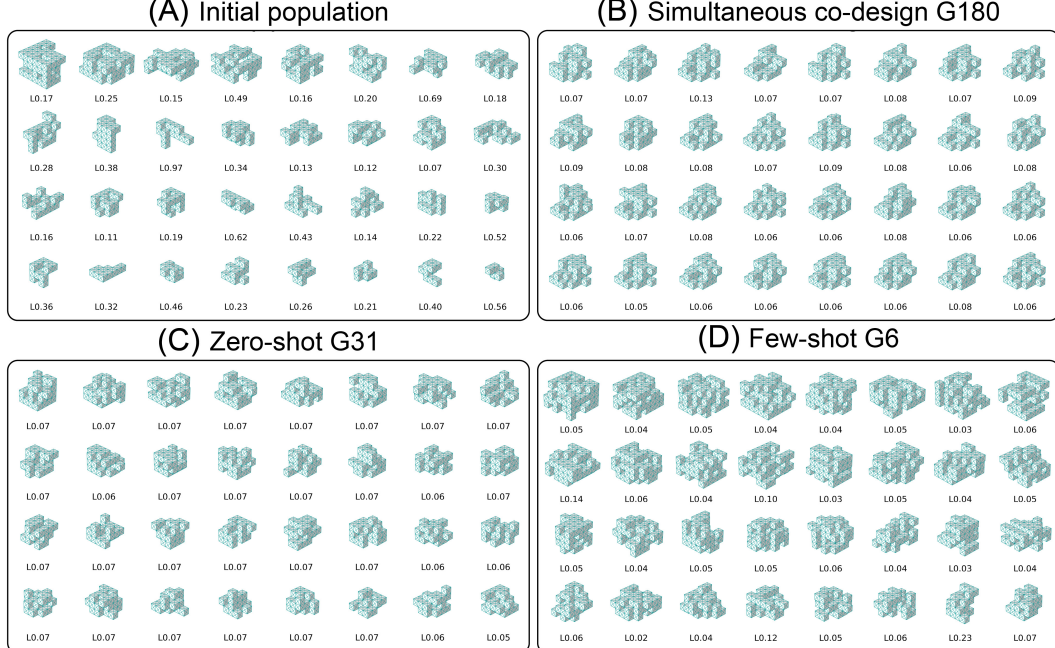


Figure 12: Morphological distinctiveness. Robot designs shown are sampled uniformly from each generation’s test performance distribution and arranged (left to right, top to bottom) by morphological distinctiveness, defined as the mean pairwise Hamming distance to its peer designs. Performance scores appear below each design. The initial population (**A**) exhibits diverse morphologies with broad performance variation, serving as the starting point for all methods. After 180 generations, simultaneous co-design (**B**) yields high-performing but morphologically homogeneous designs. In contrast, both zero-shot evolution at generation 31 (**C**) and few-shot evolution at generation 6 (**D**) achieve equal or superior performance while maintaining greater morphological diversity and complexity.



Figure 13: **Scaling morphology.** The embarrassingly parallel nature of the co-design pipeline allows the compute required to simulate 1024 robots with up to 1648 springs (i.e. a single GPU) to be redistributed for a single robot with 1,115,157 springs.

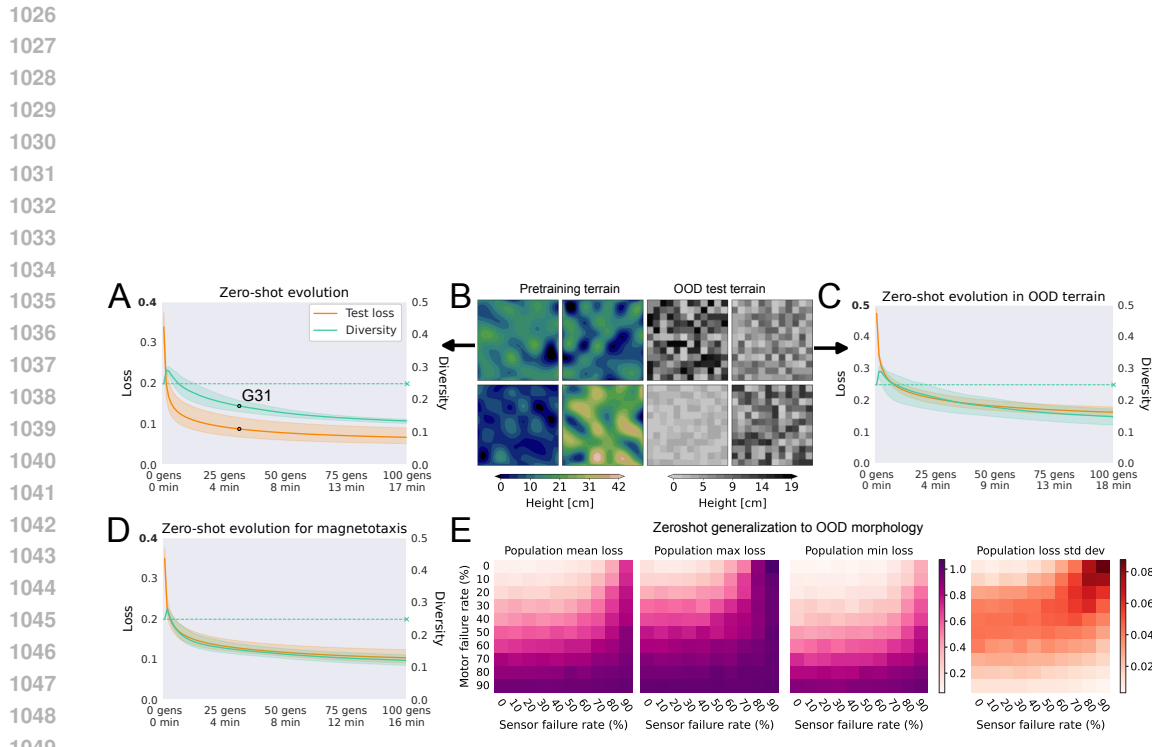


Figure 14: Zero-shot evolution, out of distribution. Without any changes to the pretrained controller, zero shot evolution rapidly improves performance by sculpting the discrete topologies of the robots in the design population through cumulative selection across generations of design mutation and recombination (A). This is true whether the distribution of terrains is similar to the continuously varying topographies experienced during pretraining (smooth blue-green maps in B) or if terrain distribution is replaced with discrete platforms of randomized height (grayscale checkerboards in B). Using the same pretrained controller, zero-shot evolution generalized to the tested out-of-distribution terrains, significantly improving upon pretraining performance (C). Next, we altered the controller’s perceptual categories by replacing one kind of sensory input (light) with another (magnetic fields), requiring the policy to generalize from the original behavior optimized during pretraining (phototaxis) to be another (magnetotaxis; D). Zero shot evolution finds designs that “undo” this perceptual shift to once again beat pretraining performance. Finally, we tested the ability of the evolved designs to generalize to out of distribution perceptual and action constraints, without any further evolution or policy finetuning (E). This last test measures the design’s robustness to sensor and motor failure, which is ubiquitous in physical robots. As in Fig. 6, evolved populations were extracted from G31, the generation at which average performance surpassed that of simultaneous co-design, the state-of-the-art benchmark from Li et al. (2025). Morphologies from G31 had their motors and sensors randomly knocked out prior to evaluation. On average, under a simultaneously high rate (60-70%) of sensor failure and a modest rate (20-30%) of motor failure, the population preserves pretraining performance. The performance differential between the best and the worst design in the population highlights the importance of maintaining a population of unique designs. The robustness of the pretrained controller to sensor and motor failure also reflects positively on potential for sim2real transfer where power constraints limit the number of actuating and sensing components and robots must withstand hardware failures.

1080 **LLM USAGE**
10811082 In a few instances, we used LLMs to refine technical language in our Methods section. The sole
1083 purpose of this was to improve succinctness and clarity for readers. LLMs only refined original
1084 content contributed by the authors and no LLM authored any new content used in this paper.
1085

1086

1087

1088

1089

1090

1091

1092

1093

1094

1095

1096

1097

1098

1099

1100

1101

1102

1103

1104

1105

1106

1107

1108

1109

1110

1111

1112

1113

1114

1115

1116

1117

1118

1119

1120

1121

1122

1123

1124

1125

1126

1127

1128

1129

1130

1131

1132

1133